3
Molecular Memory Device Based on a Tetranuclear Organotin Sulfide Cage

Research Article based on this study:

Mishra, A., Betal, A., Pal, N., Kumar, R., Lama, P., Sahu, S., and Metre, R. K., (2020), "Molecular Memory Switching Device Based on a Tetranuclear Organotin Sulfide Cage $[(RSn^{IV})_4(\mu\text{-}S)_6]\cdot 2CHCl_3\cdot 4H_2O$ (R = 2-(Phenylazo)phenyl): Synthesis, structure, DFT studies, and memristive behavior", *ACS Applied Electronic Materials*, Vol.2, No.1, pp.220–229.

3.1 Introduction

Coordination chemistry of molecular complexes has been continuously attracting interest in recent years due to the large diversity present in terms of structure, design, synthesis and interesting properties [Bellussi et al., 2012; Jones, 2003; Pandey et al., 2019; Sahoo et al., 2014; Yiu et al., 2005]. Coordination complexes consisting of transition and lanthanide metal ions are well known in the literature for their applications in the emerging technologies in important areas of molecular electronics and molecular photonics such as OLEDs, molecular wires, liquid crystalline materials, molecular switches, dye-sensitized photovoltaic cells and nonlinear optical materials [Barkhouse et al., 2015; Derrat et al., 2018; Dickie et al., 2017; Freitag et al., 2016; Liu et al., 2016; Tamer et al., 2015; Uchida et al., 2017; Zhao et al., 2016]. Molecular materials which are made up of organometallic complexes are particularly attracting interest recently due to varieties of reasons such as their ease of processing, lightweight, flexibility, solubility and extremely high versatility in terms of design, durability as active material in devices as pristine material or when present in an organic matrix [Arakaki et al., 2015; Saparov et al., 2016]. Thus, molecular organometallic complexes have attracted increasing interest as potential candidates to address various challenges in the area of molecular electronics [Camarero et al., 2009; Mitzi et al., 2001]. Memristive devices are an acronym for resistive memory devices. Usually, a conductor/semiconductor has a particular electrical resistance, but there exist some materials which have more than one resistance owing to the chemical nature (oxidation/reduction) of the material. When a material has two resistances, it can be used for assigning binary states (bits such as 0 or 1). Since these states can retain the assigned binary for a longer duration, they can be called memory elements as well. So, when material's bistable resistances are used for the fabrication of such memory devices, they are called as memristive devices. Nowadays, non-volatile memristive devices are attracting continuous attention because of their various important aspects, such as their low-cost synthesis, ease of the process, fast switching speed, a large On/Off ratio, longer stability and less power consumption [Ling et al., 2005; Yang et al., 2009]. S. Kano *et al.* have reported single molecular memory behavior at room temperature for a copper complex of porphyrin ligand containing disulfide bonds [Kano et al., 2012]. While Bandyopadhyay *et al.* have reported cobalt-based polymer containing an azo functional group, which shows the memristive behavior [Bandyopadhyay et al., 2011]. S. Pookpanratana *et al.* reported redox-active diruthenium molecular complex displaying non-volatile memory device behavior [Pookpanratana et al., 2016]. Hong *et al.* reported a phosphole oxide-based Au(III)

complex, which shows ternary memory performances [Hong et al., 2016]. Similarly, Hu *et al.* reported the multilevel memories of a polyoxometallate-based hybrid polymer with rewritable switching properties and good retention [Hu et al., 2014].

However, intriguing research is still underway to develop new strategies and molecular architectures for these advanced functional hybrid memory devices with much-improved performance. Main group molecular materials have attracted considerable research interest in the recent past owing to their vast potential applications in the areas such as catalysis, magnetism, spintronic, and optoelectronics [Bilyachenko et al., 2017; Bradley et al., 2009; Coste et al., 2019; Dufaud et al., 2003; Gabbaï et al., 2017; Kickelbick, 2007; Levitsky et al., 2019a, 2019b]. Rosemann *et al.* have reported an organotin sulfide cage that shows a very interesting photon up-conversion phenomenon whereby IR wavelength is converted into visible light [Rosemann et al., 2016a]. Recently, K. V. Raman *et al.* have reported Zn complex of phenalenyl ligand showing excellent memory device behavior [Raman et al., 2013]. However, to the best of our knowledge, a comprehensive study of organotin molecular complexes for memory device applications is not reported in the literature so far. Also, complexes bearing azobenzene moieties are known to display thermal and photochemical switching behavior in the literature. With these considerations and well-known evidence from the literature that azobenzene moiety bearing coordination complexes [Goswami et al., 2014, 2017b; Paul et al., 2012] display interesting electrical properties, this chapter focuses on the design and synthesis of tetranuclear organotin sulfide cage by exploiting intramolecular coordination approach using 2-phenylazophenyl as an organic substituent on tin.

3.2 Experimental Section

3.2.1 Synthesis

***[(RSn^{IV})$_4$(μ-S)$_6$]·2CHCl$_3$·4H$_2$O (R = 2-phenylazophenyl) (1)*:** A suspension of $RSnCl_3$ (R = 2-phenylazophenyl) (0.10 g, 0.25 mmol) and $Na_2S{\cdot}9H_2O$ (0.088 g, 0.37 mmol) in 20ml of acetone/methanol (1:1) was stirred at 0-5 ºC for 4 hr. The suspension was filtered and kept for complete evaporation at room temperature resulting in a yellow solid which was dissolved in chloroform and X-ray quality crystals of **1** were grown from the slow evaporation of chloroform solvent. Yield (Based on Sn): 0.073g (86%). M.P. >260ºC (dec.), Anal. Calcd for $C_{48}H_{36}N_8S_6Sn_4$ C, 41.42; H, 2.61; N, 8.05; S, 13.82 Found: C, 42.72; H, 2.04; N, 7.43; S, 13.60. ^{1}H NMR (500MHz, $CDCl_3$, ppm): δ 8.8 (d), 8.16 (d), 8.01 (d), 7.6 (m), 7.4 (m). ^{13}C{^{1}H}NMR (125MHz, $CDCl_3$, ppm):δ 152, 148, 135, 133, 132.7, 132.4, 131, 129, 125. ^{119}Sn NMR (186MHz, $CDCl_3$, ppm): δ -98. ESI-MS: $[(RSn)_3S_4]^+$ 1028.831; IR (KBr, cm^{-1}): 3064 (m), 1694 (w), 1586 (w), 1210 (m), 1103 (w), 780 (s), 673 (m), 539 (m).

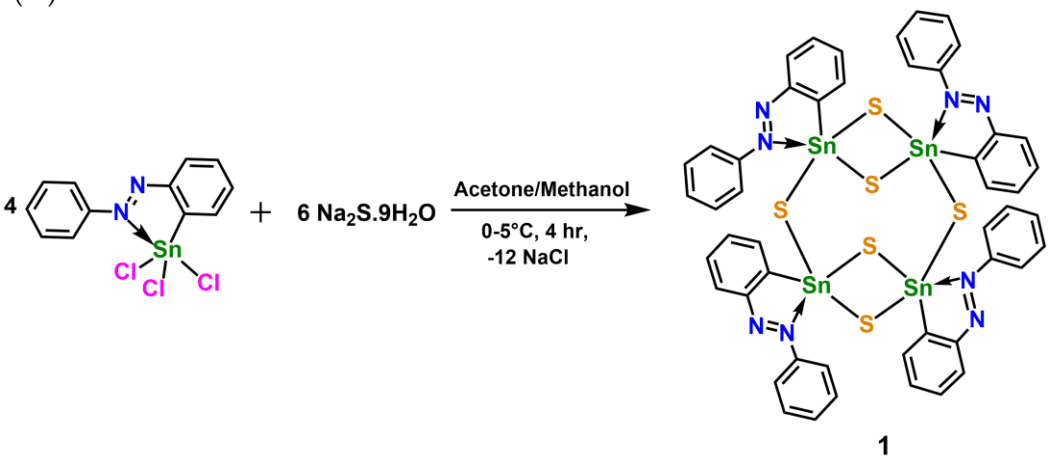

Scheme 3.1. Synthesis of complex **1**.

3.2.2 Single-Crystal X-ray Crystallography

The details of the data collection and refinement for **1** are given in Table 3.1. As the solvent molecules were disordered with high thermal factor values even at 100 K, squeeze analysis was performed using Program PLATON [Spek, 1999] and the squeeze result was appended to the

CIF file. The squeeze analysis shows that there are 639 electrons present per unit cell. Each unit cell contains 16 metal centers, and as per asymmetric unit (monoclinic crystal system, space group P2/n), only 4 metal centers are present. Therefore, the total number of electrons present per asymmetric unit is 639/4 electrons, roughly corresponding to two chloroform molecules and four water molecules per asymmetric unit in the cavity.

Table 3.1 Crystal data and structure refinement parameters for complex **1.**

Identification code	**1**
Empirical formula	$C_{50}H_{46}Cl_6N_8O_4S_6Sn_4$
Formula weight	1502.87
Temperature/K	100(2)
Crystal system	monoclinic
Space group	P2/n
a/Å	15.043(13)
b/Å	22.327(18)
c/Å	20.445(17)
α/°	90
β/°	93.292(11)
γ/°	90
Volume/Å^3	6856(10)
Z	4
ρ_{calc}g/cm^3	1.349
μ/mm^{-1}	1.655
F(000)	2704.0
Crystal size/mm^3	0.220 × 0.200 × 0.160
Radiation	MoKα (λ = 0.71073)
2Θ range for data collection/°	2.704 to 50
Index ranges	-17 ≤ h ≤ 17, -26 ≤ k ≤ 26, -24 ≤ l ≤ 24
Reflections collected	143104
Independent reflections	12078 [R_{int} = 0.0498, R_{sigma} = 0.0216]
Data/restraints/parameters	12078/0/595
Goodness-of-fit on F^2	1.018
Final R indexes [I>=2σ (I)]	R_1 = 0.0213, wR_2 = 0.0461
Final R indexes [all data]	R_1 = 0.0316, wR_2 = 0.0509
Largest diff. peak/hole / e Å^{-3}	0.60/-0.28

3.2.3 Memory Device Fabrication

Metal-Insulator-Metal (MIM) sandwich structure was fabricated using complex **1** as the active material between two metal contacts, namely ITO and Aluminium. ITO coated glass was purchased from Techinstro and used as a substrate for memory device fabrication. To get a thin strip of ITO at the middle portion, glass substrates were etched with Zn dust and concentrated hydrochloric acid [Vyas et al., 2016]. To clean the etched substrates, they were ultrasonicated in soap solution followed by De-ionized (DI) water three times for 15 min each. Then three ultrasonication cycles were performed with acetone, DI water, and methanol for 15 min each [Vyas et al., 2018a]. Cleaned substrates were kept in an incubator at 70° C for 5 h.

As synthesized, complex **1** was dissolved in chloroform after a few hours of ultrasonication to give rise to a homogeneous mixture. The thin film on the ITO substrate was

obtained by spin coating at 2000 rpm, and after that, the thin film was vacuum dried for 7-8 hrs. Polystyrene (PS) was mixed as a matrix material with complex **1** by the weight ratio of 40:60 (PS: Complex 1) to get a better consistency. The aluminium metal was purchased from Sigma-Aldrich and deposited on the film using thermal evaporation. The thickness of the deposited aluminium is about 70 nm. So, two types of device structures were fabricated, one is Al/Complex **1**/ITO denoted as D1, and the other is Al/PS:Complex **1**/ITO denoted as D2. The device structure is shown in Fig. 3.1. The devices were electrically characterized using a Keithley 6430 Femto ampere source meter.

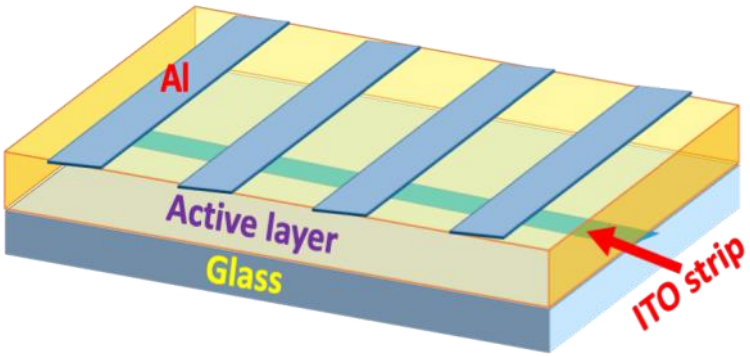

Fig. 3.1 Schematic diagram of the device in which complex **1:** PS (60:40) is used as an active layer.

3.2.4 Theoretical Calculations

Density functional theory (DFT) calculations were carried out using Gaussian 09 [Frisch et al., 2009] suite of programs. The geometry optimization was performed at TPSSH functional [Dirac, 1929; Dornsiepen et al., 2017; Frisch et al., 2009; Perdew et al., 2018; Slater, 1951; Staroverov et al., 2003; Tao et al., 2003] with def2-SVP basis set (TPSSH/def2-SVP) for all the atoms. The single point energy calculation on the optimized geometry was done using def2-TZVP basis set [Weigend et al., 2005]. The UV-vis absorption spectra were calculated on the DFT optimized geometry of complex **1**, using ORCA 4.0.1 program [Neese, 2012] with TDDFT method. Here, we have used the TPSSH/def2-TZVP basis set with RIJCOSX approximation. The solvent effect was considered using CPCM method with DCM.

3.3 Results and Discussion

3.3.1 Synthetic Aspects

The reaction of $RSnCl_3$ (R = 2-phenylazophenyl) with 1.5 molar equivalent $Na_2S{\cdot}9H_2O$ gave the organotin sesquisulfide $[(RSn^{IV})_4S_6]$, **1**, as crystalline material. Single-crystals suitable for X-ray diffraction were obtained as its $CHCl_3$ and H_2O solvate **1**$\cdot 2CHCl_3 \cdot 4H_2O$ (Scheme 3.1). The ^{119}Sn NMR spectrum of the complex recorded in $CDCl_3$ showed a single resonance at δ = -98 ppm, indicating all the four Sn atoms present in the complex are in the same chemical environment. The ^1H NMR spectrum showed signals in the region δ = 7-9 ppm, which can be attributed to the aromatic protons present in 2-phenylazophenyl attached to the Sn center (Fig. 3.2). ESI-MS studies of complex **1** reveal the absence of a molecular ion peak; however, a peak at m/z 1028.831 can be assigned to fragment $[(RSn)_3S_4]^+$. Thermogravimetric analysis revealed that after initial weight loss due to solvent of crystallization, the complex **1** is stable up to 290^{o}C, after which it undergoes sudden weight loss (Fig. 3.3).

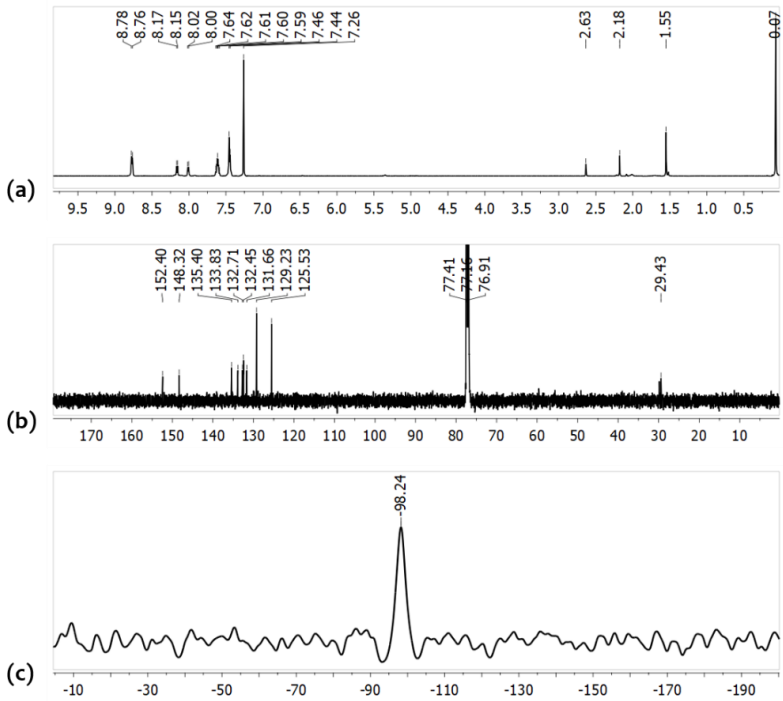

Fig. 3.2 (a) ^{1}H NMR, **(b)** ^{13}C NMR and **(c)** ^{119}Sn NMR of complex **1** recorded in $CDCl_3$.

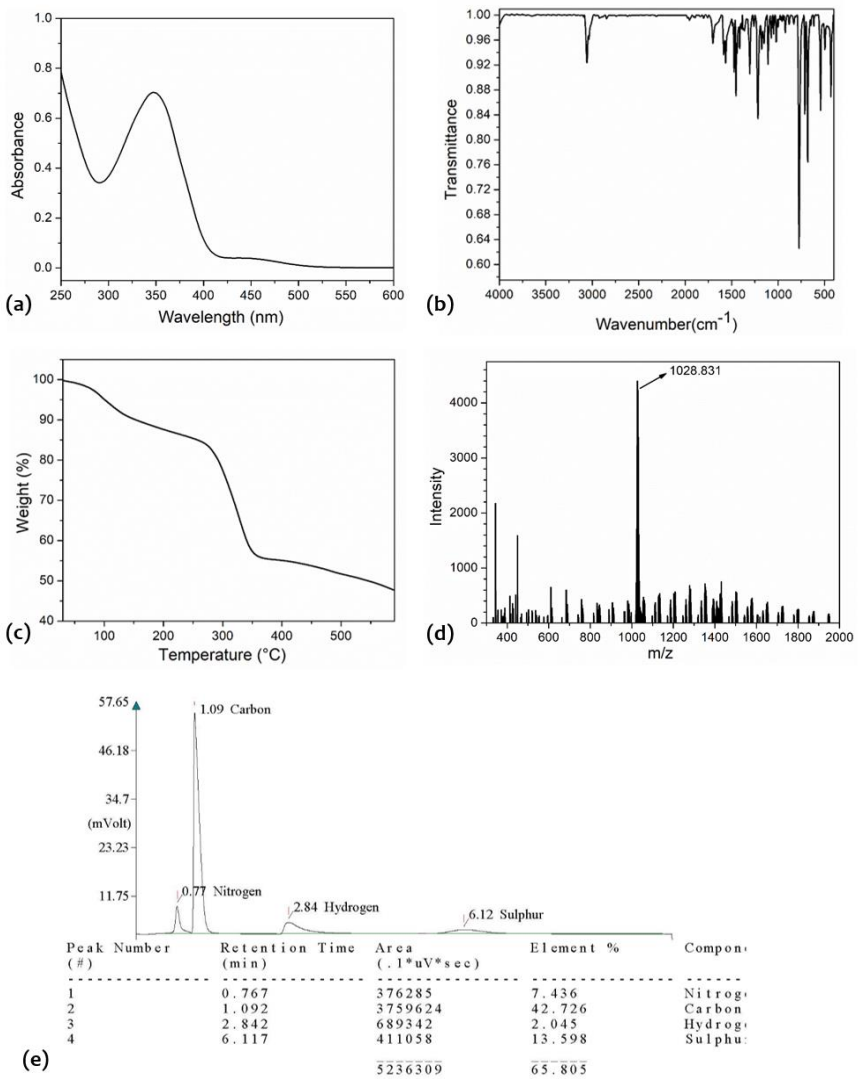

Peak Number (#)	Retention Time (min)	Area (.1*uV*sec)	Element %	Compon
1	0.767	376285	7.436	Nitrog
2	1.092	3759624	42.726	Carbon
3	2.842	689342	2.045	Hydrog
4	6.117	411058	13.598	Sulphu
		5236309	65.805	

Fig. 3.3 (a) FTIR spectrum, **(b)** UV-Vis spectrum (conc. 10^{-5}M in $CHCl_3$), **(c)** TGA (under N_2 atmosphere) **(d)** ESI-MS spectrum and **(e)** CHN analysis for complex **1.**

3.3.2 Molecular and Supramolecular Structure of Complex 1

The molecular structure of complex **1** is shown in Fig. 3.4(a). Complex **1** has a cage-like structure with a Sn_4S_6 central core. The central Sn_4S_6 core consists of four Sn centers bridged by six μ-S ligands. The cage-like structure in **1** comprises upper and lower Sn_2S_2 rings which are held together by two bridging μ-S ligands forming a double-decker like core structure. The asymmetric unit of **1** consists of two crystallographically unique $[(RSn)_2S_3]$ units. All the tin centers of the Sn_4S_6 core are not present in the same plane [Fig. 3.4(b)]. Two tin centers (Sn1, Sn1′) lie below the plane, while the other two tin centers (Sn2, Sn2′) lie above the plane. The average Sn-S-Sn bond angle in two Sn_2S_2 rings is 86.79° which is smaller than the average Sn–S–Sn bond angle (108.72°) connecting two Sn_2S_2 units through bridging μ-S ligands. The Sn–S bond distances of the four-membered rings are Sn(1)-S(2), 2.4001(1) Å and Sn(1)-S(3′), 2.4817(1) Å, which are in close agreement with similar Sn_4S_6 core containing complexes reported earlier [Berwe et al., 1987; Dakternieks et al., 1993; Fard et al., 2009a]. Each tin center in **1** is also further bonded to 2-phenylazophenyl substituent involving intramolecular N→Sn interaction, which appears to play an important role in stabilizing the Sn_4S_6 core. The N→Sn bond distances observed in **1** [average 2.584 Å] are slightly longer than those found in the starting material $RSnCl_3$ (R=2-phenylazophenyl), 2.451(2) Å [Chandrasekhar et al., 2013a]. Intramolecular N→Sn distances in **1** are comparable with the organotin sulfide complexes reported earlier [Jurkschat et al., 1992; Trimeres et al., 1991]. Each Sn atom in **1** is pentacoordinated [1C, 1N, 3S coordination], possessing a distorted trigonal bipyramidal geometry with an intramolecularly coordinated N1 and S3′ atoms at the axial position and C12, S1 and S2 atoms at equatorial position [Fig. 3.4(c)]. Addison's tau parameter in this instance found to be, τ = 0.75 (τ = 1 for perfect trigonal bipyramidal geometry) [Addison et al., 1984; Kaya et al., 2019].

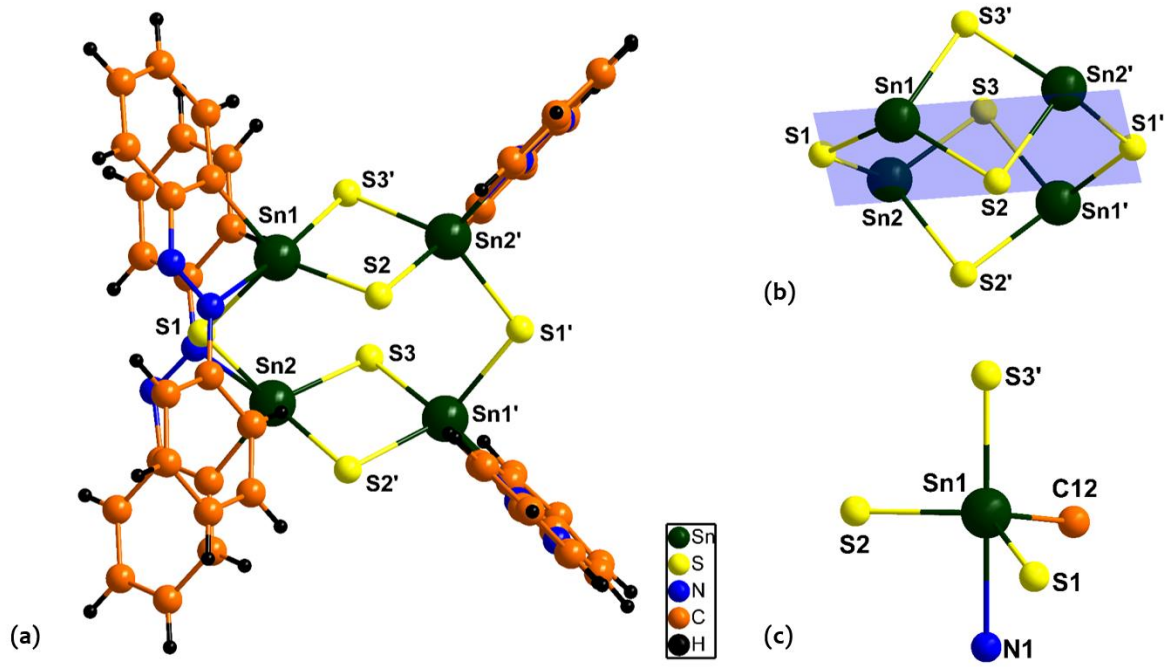

Fig. 3.4 (a) Molecular structure of complex **1**. Bond distance (Å) and bond angle (°) parameters: Sn1-S1, 2.4177(1); Sn1-C12, 2.1316(3); Sn2′-S2, 2.4775(1); Sn1-S1-Sn2, 108.727(5)°; Sn1-S3′-Sn2′, 86.825(5)°; **(b)** Sn_4S_6 core structure with a plane passing through two S atoms (S1 and S1′); **(c)** coordination environment of Sn in complex **1**; Sn1-S3′, 2.4816(1); Sn1-S2, 2.4001(1); Sn1-N1, 2.5657(2); C12-Sn1-S3′, 103.142(9)°, N1-Sn1-S1, 84.243(6)°; N1-Sn1-C12, 70.144(1)°; N1-Sn1-S3′, 169.838(8)°; S2-Sn1-S1, 124.835(5)°.

Previous reports in the literature on organotin complexes show that they form interesting supramolecular structures in the solid-state through non-covalent interactions [Chandrasekhar et al., 2005, 2007; Leusmann et al., 2015]. Accordingly, a closer analysis of the X-ray crystal structure of **1** revealed the formation of two-dimensional supramolecular architecture as a result of several intermolecular C-H…π, π…π and C-H…-S interactions (Fig. 3.5 and 3.6).

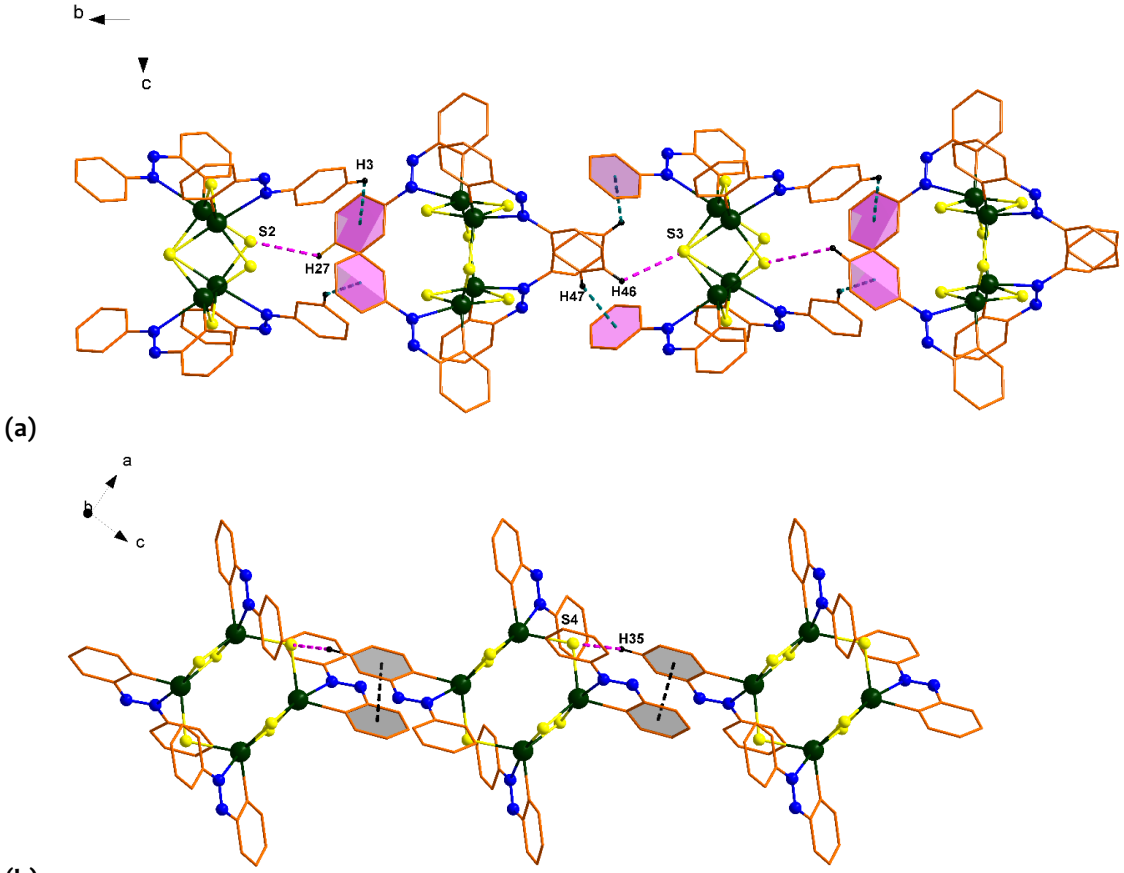

Fig. 3.5 (a) One-dimensional supramolecular assembly of **1** formed by CH…π, S…H interactions. Metric parameters are as follows; π-H3, 3.6052(2) Å; π-H47, 2.7356(1) Å; S3-H46, 3.1859(2) Å; S2-H27, 3.5054(2) Å; **(b)** One-dimensional supramolecular assembly formed by π…π, S…H interactions. Metric parameters are as follows; π-π, 3.7640(2) Å; S4-H35, 3.1715(1) Å.

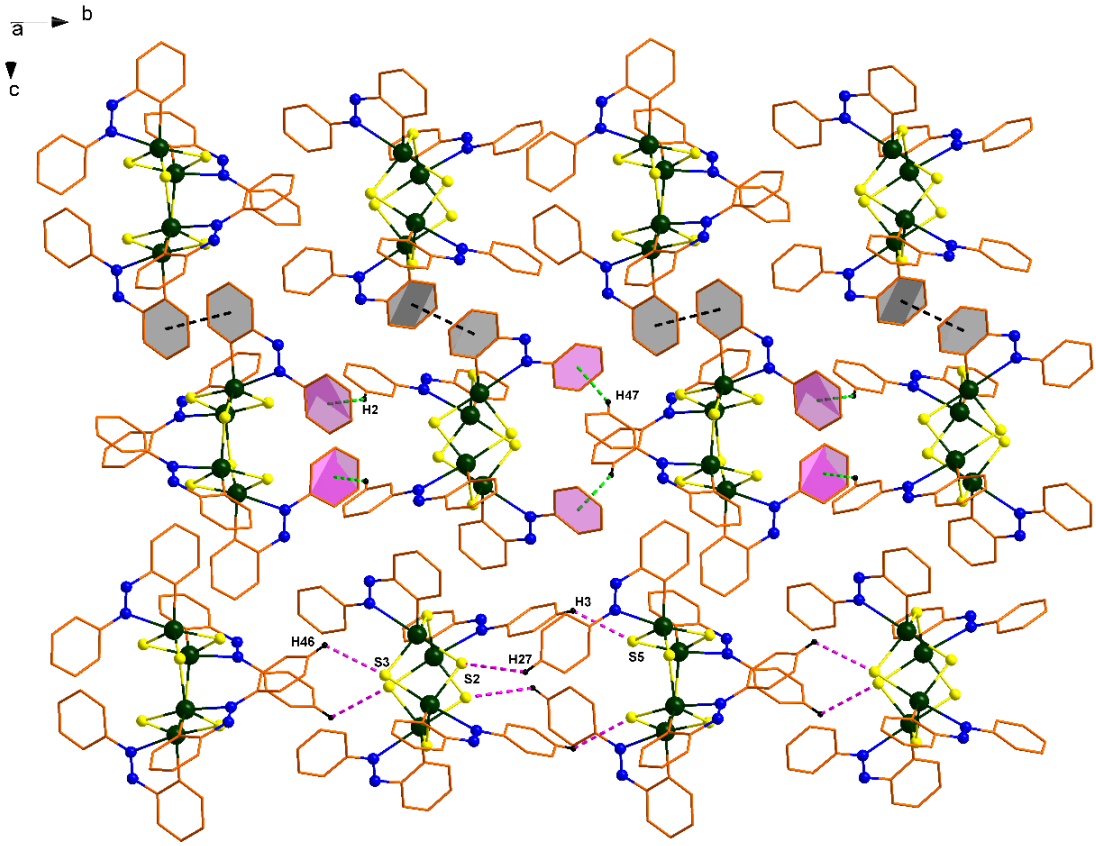

Fig. 3.6. Two-dimensional supramolecular architecture of **1** formed by CH…π, π…π, S…H interactions. Metric parameters are as follows; π-π, 3.7283(2)Å; π-π, 3.7640(2)Å; π-H47, 2.7356(1)Å; π-H42, 2.8738(1)Å; S5-H3, 3.1036(2)Å; S2-H27, 3.5054(2)Å; S3-H46, 3.1859(2)Å.

3.3.3 Photophysical and DFT Studies

The UV-visible spectrum for complex **1** was recorded at room temperature with 10^{-5} M concentration in chloroform. The spectrum shows two peaks, one at 347 nm with a larger extinction coefficient and another small peak at 442 nm. The peak at 347 nm may be associated with symmetry allowed due to the 2-phenylazophenyl based π – π* transition. To fully understand these peaks, the time-dependent density functional theory (TD-DFT) calculation was performed on this complex in collaboration. TD-DFT calculation also suggests two characteristic peaks at 366 nm and 432 nm, which are in agreement with the experimental UV-Vis data (see Fig. 3.7). As expected, the transition at 366 nm is found to be π – π* within 2-phenylazophenyl moiety and the transition at 432 nm corresponds to the non-bonding orbital of sulfur (n) to π*-orbital of 2-phenylazophenyl moiety (n – π*) which is generally found to have low extinction coefficient.

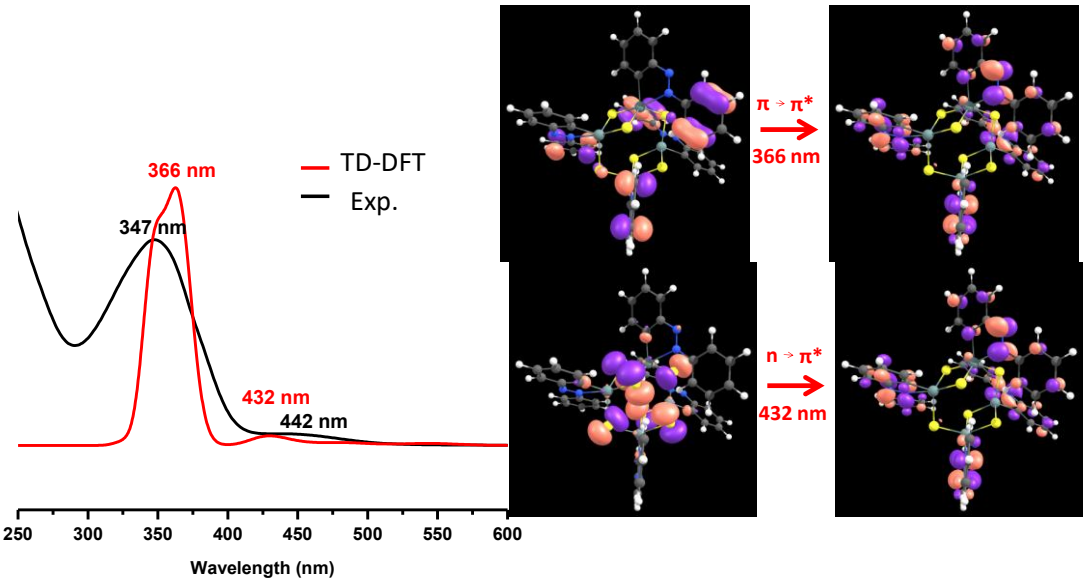

Fig. 3.7 Computed absorption spectra (in red) of complex **1** using TD-DFT calculations and its corresponding orbitals involved in the transitions. The experimental spectrum of **1** is given in the black line for comparison.

To have a closer look at complex **1**, the highest occupied molecular orbital (HOMO) and lowest unoccupied molecular orbital (LUMO) were computed using DFT calculations. The DFT calculated energies for HOMO and LUMO of complex **1** are found to be -5.99 eV and -2.94 eV, respectively, which give rise to the HOMO-LUMO energy gap of 3.05 eV for this complex. Both HOMO and LUMO have ligand characters (see Fig. 3.8). The HOMO involves the pure non-bonding p-orbital of sulfur atoms, while LUMO consists of π* of 2-phenylazophenyl ligand, which suggests the transition observed at 432 nm in TDDFT is a HOMO to LUMO transition. The above calculations suggest that complex **1** will be a promising candidate for memory device application as it involves mainly ligand-based transitions [Ling et al., 2006; Xie et al., 2008].

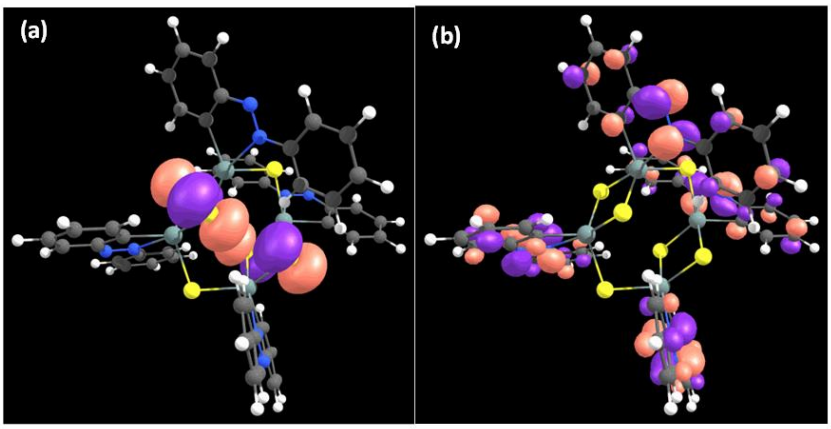

Fig. 3.8 Diagram shows the **(a)** HOMO and **(b)** LUMO orbital pictures of complex **1**. The orbital with orange color represents the alpha orbital and the violet color with a beta orbital. The contour value used to plot these is 0.03 a.u.

3.3.4 Memory Device Behavior Studies

Device studies were performed in collaboration. Two devices, D1 (ITO/complex-**1**/Al) and D2 (ITO/Complex-**1**:PS/Al), were studied to understand the electrical behavior of the material in its pristine form and inside an insulating matrix. I-V characteristic of device D1 and D2 was studied for a better understanding of the electrical properties of the materials in the device. Fig. 3.9(a) shows the I-V curve of D1, for which the voltage was swept from 0 V to 2.5 V and then back to 0 V and the same thing is performed in the negative direction as well to complete the loop. In this process, a scan rate of 0.1 V/s was set for a smooth I-V curve without any contribution from the space charge. The current of the device increases with voltage and at 2.5V current reaches the maximum. The on-off ratio of current in Low Resistance State (LRS) to High Resistance State (HRS) was found to be ~10. Hundreds of such sweeps have been taken, and the device seems to follow the same trend with the same magnitude of current in both positive and negative directions, which suggests that the device is stable. Since the device on-off ratio is not very high, so a different device structure called D2 was fabricated. I-V characteristics of D2 were taken from a low voltage range (from 0.2 V) and increased at a step of 0.2 V with a scan speed of 0.02 V/s, but no switching was observed up to 0.8 V and remained in the HRS. At 1V, the device starts showing switching, but the on-off ratio and consistency were not so good. As the voltage increased to 1.4 V, i.e., voltage sweeps from -1.4 V to 1.4 V device shows consistent switching iterations with the on-off ratio of the order of 10^3, as shown in Fig. 3.9(b). For this device also, hundreds of sweeps to check the consistency and stability of the device were performed, and indeed, the device showed unprecedented stability. The device was in the HRS at first; after -0.42 V current starts increasing indiscriminately, which indicates the contribution of space charge. At -1.4 V current reached the maximum (LRS) and stayed in that state even when the voltage decreased. For the voltage sweep from 0 V to 1.4 V, the device was in the LRS and as the voltage increased, negative differential resistance (NDR) behavior was observed and consequently HRS or erase state of the device reached 1.4 V, which tells that the device can be used as flash memory.

Random-access memory (RAM) behavior was studied by the Write-Read-Erase-Read cycle where -1.4V and 1.4V were applied as write and erase voltages, respectively, and the corresponding behavior is shown in Fig. 3.9(c). A -0.25V pulse was applied to read the difference between write and erase states. Write, read and erase pulses were applied for 10 s in each pulse, i.e., a total of 40 s for every cycle. More than 2500 cycles were considered, and RAM behavior was found to be consistent. Read-only memory (ROM) behavior has also been checked by studying its stability at a particular conducting state. To check the LRS state, a write pulse of -1.4V was applied for 10 s to the device and after that, a small pulse of -0.25V as a read voltage was applied for more than 10000 s to check the retention of the high current state. Similarly, a +1.4V pulse was applied as an erase voltage for 10 s to change the conducting state of the device from LRS to HRS and hence to check its retention capability. ROM was recorded for more than 10^4 s, and it shows a good stable conducting state, as shown in Fig. 3.9(d). At LRS and HRS, the currents are about 10^{-6} Ampere and 10^{-8} Ampere.

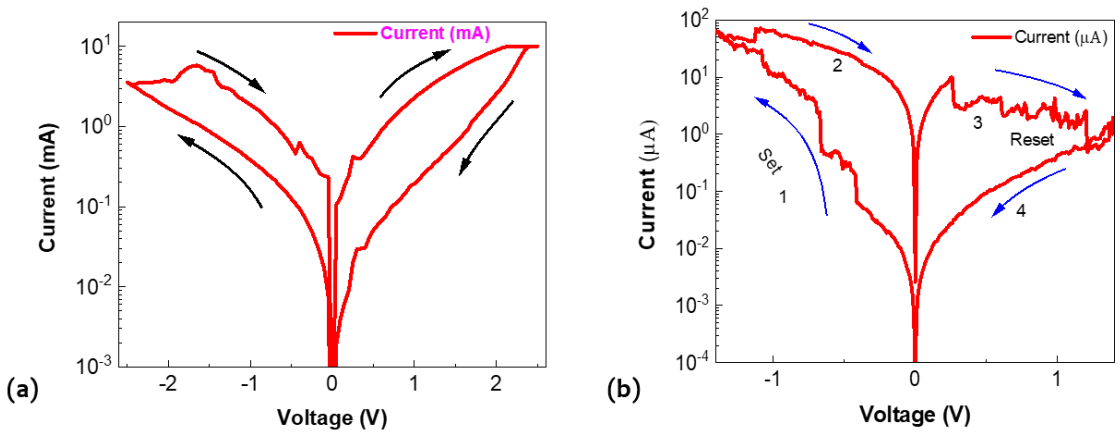

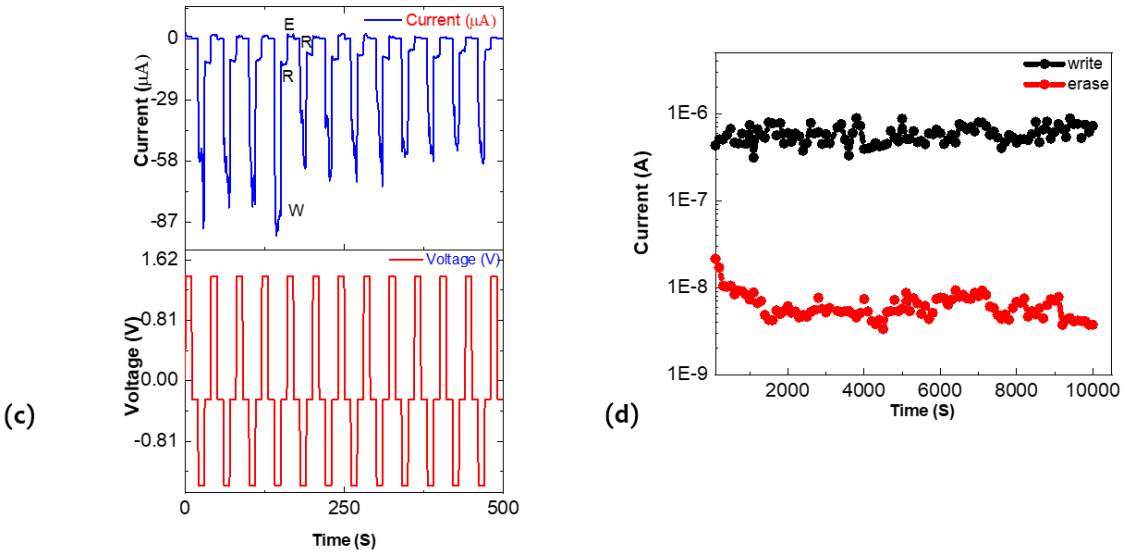

Fig. 3.9 I-V characteristic curve of the devices in which an active layer as **(a)** Complex **1** **(b)** Polystyrene mixed with complex **1** (40:60) as a matrix was used, the black and blue arrows show the current direction during voltage sweep. **(c)** Write-read-erase-read sequence to check the consistency of writing and erasing state. Writing pulse was given at -1.4V for 10 s and erasing voltage was given at 1.4V for 10 s. All the states were read at -0.25V for 10 s, i.e., 40 s were taken to complete one cycle. More than 2500 such cycles were taken to check consistency and the device was found to be consistent **(d)** After giving a write pulse and erase pulse at -1.4 V and 1.4 V respectively, testing of stability at a particular state was done by giving a constant reading pulse at -0.25 V for 10000 S.

The surface morphology of the devices was studied by Park system XE 70 Atomic Force Microscope (AFM). The thin films of the active layer were prepared for taking AFM images in the same environment and conditions in which devices were fabricated. All studies were performed in non-contact mode with a scan speed of 0.5nm²/s to get the best image. The scan was started on a 10μm x 10μm area for both devices. Large humps and cracks can be seen on the surface of the D1 device, so a smaller area was zoomed in. Fig. 3.10(a) shows the AFM image of an active layer of D1 in which a good plane surface for very small areas was obtained (typically 1μm x 1μm area). The roughness (RMS) in the whole region of the D1 surface is 1.201 nm. AFM image of the D2 device shows that the surface is mostly planer, although it contains some clusters and pinholes, as shown in Fig. 3.10(b). The surface roughness (RMS) for this device is 3.721nm, and though the roughness is more than the pristine device surface, it is relatively better than the first one. Small clusters are seen on the surface with a height profile of about 2-10 nm, as shown by the circle. The small pinholes are shown by a square through which the metal ions can penetrate.

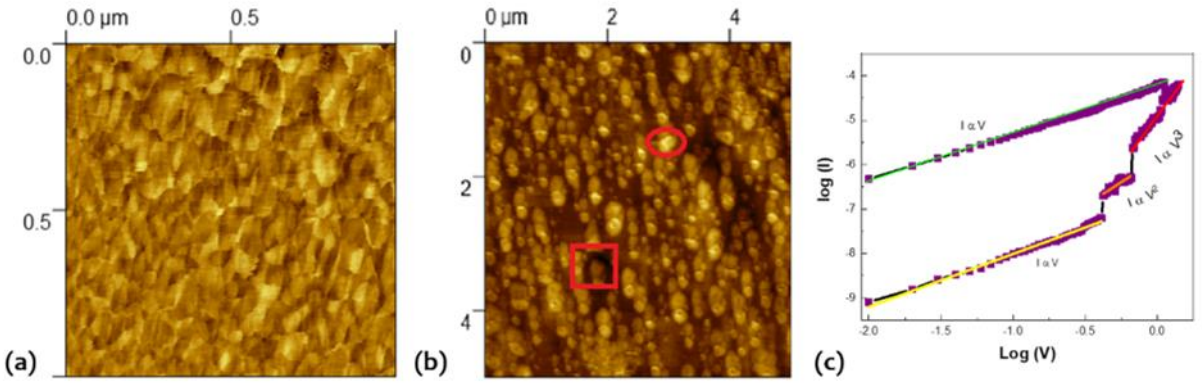

Fig. 3.10. AFM image of the device **(a)** image of complex **1** on 1μm x 1μm area **(b)** image of the complex **1** and PS material on 5μm x 5μm scan area. These devices are prepared in the same environment and concentration. **(c)** Fitting of current vs. voltage curve in logarithm scale with voltage sweep starts from 0V to -1.4V again to 0V. Fitting shows the different regions of current conduction.

The possible current conduction mechanisms that can describe the resistive switching include thermionic emission [Chen et al., 2017], charge trapping [Lampert, 1956], ohmic conduction [Liu et al., 2009], filament formation and ion migration [Gu et al., 2016; Wang et al., 2018] and space charge limited conduction (SCLC) by filling the defect states [Zhang et al., 2017b]. To describe the mechanism, the HRS to LRS switching sweep from 0V to -1.4V to back to 0V on a logarithmic scale was plotted for both current and voltage, as shown in Fig. 3.10(c). From 0V to -0.41V (-2 to -0.387 along the x-axis on a logarithmic scale) shows that HRS and current vary linearly with respect to the voltage ($I \alpha V$). The fitted line (yellow line) in that region has a slope close to 1, and this confirms that it follows an ohmic conducting mechanism. So, at the low voltage, the conduction is due to the thermal energy gained by the electron. The number of electrons that pass through the barrier is less; hence, the current is very less. From -0.42V to -0.66V (-0.3767 to -0.1804 along the x-axis on the logarithmic scale) current starts increasing and the slope of the fitted line (orange line) is about two which means conducting current is proportional to the square of voltage ($I \alpha V^2$) showing SCLC by following child's law. Voltage ranges from -0.67V to -1.4V (-0.1739 to 0.1461 along X-axis in logarithmic scale) obeys trap-free SCLC ($I \alpha V^n$, n is greater than 2). Defect states in the active layer start filling by charges when voltage increases and electrons start hopping from one defect state to another to reach metal contact. For this type of conduction process, the current density equation derived by Lampert and Mark is given below [Lampert et al., 1970];

$$J = [(9N\mu\varepsilon)/8n]V^2/L^3 \quad \ldots\ldots\ldots\ldots\ldots (1)$$

Where J is current density, N is the free charge density, n is the number density of charge in trap state, ε is dielectric constant, μ is the mobility of charge carrier, V is the applied voltage and L is the thickness of the active layer. After the SCLC region, the defect states are partially filled, so the current increases gradually. For the voltage sweep from -1.4V to 0V, the current stays in the high conducting state and follows Ohm's law again, as Fig. 3.10(c) shows the slope of the fitted line (green line) is close to 1. When all defect states are filled by charge particles, conduction can take place smoothly through the active layer like a conductor and hence it follows the linear equation ($I \alpha V$) (Fig. 3.11).

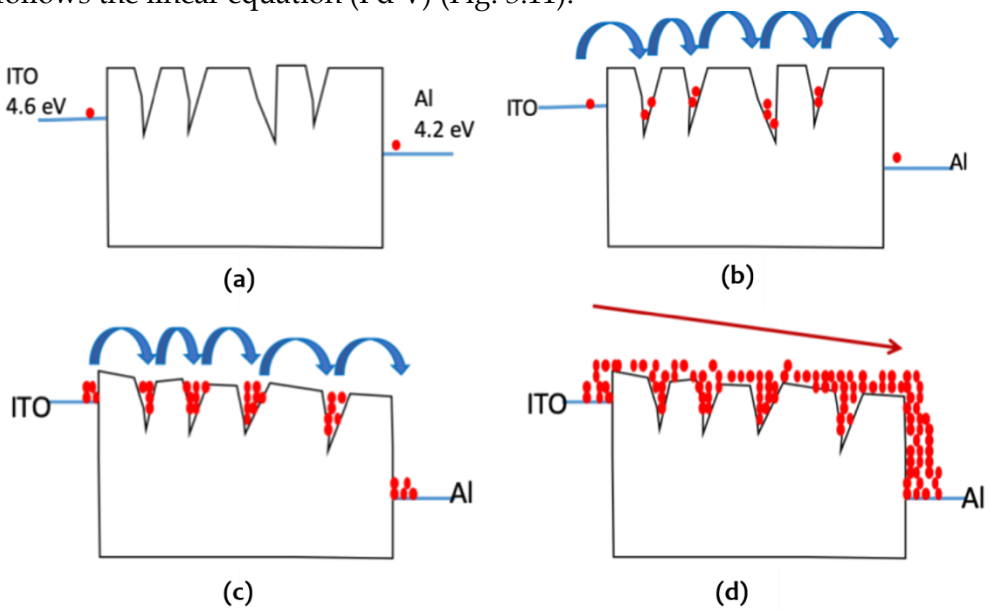

Fig. 3.11. Band diagram for current conducting mechanism **(a)** conduction current due to thermally excited charge carriers (red balls) which can tunnel the barrier are very less in number and Ohm's law was followed. **(b)** Defect states are partially filled, and charge carriers follow Child's law ($I \alpha V^2$). **(c)** The defect states are almost filled, so the SCLC mechanism ($I \alpha V^n$) was followed. **(d)** All the defect states are partially filled, and the charge carrier makes the conduction path, and again, Ohm's law was followed.

Along with these mechanisms, the contribution of metal ion penetration cannot be ruled out. Since the surface morphology study shows that a large number of pinholes and cracks are

there on D1 film so aluminium ions can penetrate through the holes; as voltage increases conducting filaments are formed at high voltages. Compared with D1, the surface of D2 has a smooth surface over a large area and has a smaller number of holes. So, the SCLC mechanism dominates the contribution of ion migration for D2. Mixing of PS in pristine solution increases the number of defect states in D2, causing dominating SCLC with a high on-off ratio and low voltage requirement.

3.4 Conclusion

In summary, a new tetranuclear monoorganotin sulfide cage $[(RSn^{IV})_4(\mu\text{-}S)_6]\cdot 2CHCl_3 \cdot 4H_2O$ (**1**) R= 2-Phenylazophenyl, has been synthesized and structurally characterized by single-crystal X-ray crystallography. Further, complex **1** is also characterized by IR, UV-Vis, TGA, ESI-MS, ^{119}Sn, ^{1}H and ^{13}C NMR spectroscopy. Complex **1** has a Sn_4S_6 central core forming a double-decker cage-like structure. DFT studies revealed the nature HOMO and LUMO orbitals of complex **1**, which are mainly ligand oriented, suggesting its promising nature for the molecular memory device. Fabrication of MIM sandwiched structure resistive memory device by mixing PS with complex **1** revealed that switching properties become better than device D1. The devices showed excellent memory behavior with a low write voltage of about -1.4V and high on/off ratio of about 10^3, long data retention of over 10000s, and good RAM properties of over 2500 cycles. Thermionic emission, ohmic conduction, metal ion migration, and SCLC mechanism are the causes of switching in the device. SCLC mechanism dominating charge transport required low voltage. The ease of fabrication, simple device structure, and outstanding performance suggest that the complex **1** can be a good candidate for resistive memory application. Complex **1** is the first organotin complex known to exhibit such memristive behavior.

…